Journal of Materials Chemistry A

RSC Publishing

PAPER

View Article Online
View Journal | View Issue

Cite this: J. Mater. Chem. A, 2013, 1, 11820

Fabrication of $SrTiO_3$–TiO_2 heterojunction photoanode with enlarged pore diameter for dye-sensitized solar cells†

Chang Woo Kim,‡[a] Sang Pil Suh,‡[a] Mi Jin Choi,[b] Yong Soo Kang[b] and Young Soo Kang*[a]

Received 4th July 2013
Accepted 29th July 2013

DOI: 10.1039/c3ta12604h

www.rsc.org/MaterialsA

We have demonstrated the N719 dye-$SrTiO_3$–TiO_2 system for the application in dye-sensitized solar cells, which is thermodynamically more favorable for electron transport and charge separation efficiency. The heterojunction $SrTiO_3$–TiO_2 photoanode with an enlarged pore diameter was fabricated by anodization of a Ti foil substrate and sequential hydrothermal reaction. Their photoelectrochemical properties were investigated as dye-sensitized solar cells for the first time. The optimal conditions for enlarged pore diameter of anodized TiO_2 nanotube arrays (TNTAs) were suggested using a tetraethylene glycol based electrolyte, and $SrTiO_3$ for the heterojunction photoanode was hydrothermally reacted on TNTAs. The structure and pore size of the hetero-structured $SrTiO_3$–TiO_2 nanotubes arrays (ST-TNTAs) were studied comparatively for their photocatalytic activity in parallel with various $SrTiO_3$ morphologies. The enhanced photocatalytic property of ST-TNTAs compared with TNTAs could be attributed to the enhanced suppression of charge recombination by the heterojunction of ST-TNTAs due to easier crossing of the interface of ST-TNTAs by more the negative conduction band potential of $SrTiO_3$. This is also possible because of the optimized interfacial area and the distance between $SrTiO_3$ nanoparticles and TNTAs. With electrochemical impedance spectroscopy, we report promising applications of dye-sensitized solar cells with the hetero-structured photoanode of ST-TNTAs for the first time.

Introduction

Since the first endeavor of Fujishima and Honda on the TiO_2 photocatalyst in 1972,[1] dimension-designed photocatalysts have been attracted numerous attention for their enhanced photocatalytic properties from their high surface area, size dependent properties and special photoreactive facets in the field of photoelectrochemical cells (PECs).[2] Considering the dimensions from nano-to micro structured materials, one-dimensional (1D) structures such as wires, tubes and rods have been successfully applied for efficient light-harvesting and charge separation in PECs.[3] By comparison to randomly arranged nanoparticle systems which show limitations of cell performance arising from a relatively high electron–hole recombination rate,[4] the vertically oriented nature of 1D structures has exhibited an extremely improved energy conversion efficiency from their direct electron and ion diffusion pathway between interfaces.[5,6] Recently, P. Yang's group reported an increased rate of electron transport through the nanowire geometry of a 1D ZnO nanowire array.[6] A. J. Frank determined that the charge collection efficiency of the 1D nanotube was markedly enhanced because of their slower recombination rate. They also reported on the relationship between the morphology and electron dynamics of oriented TiO_2 nanotube arrays.[7] C. A. Grimes' group suggested the 1D TiO_2 nanotube showing remarkable photoconversion efficiency as their promising photoanode.[8] This trend revealed that the 1D structured photoanode in PECs allowed significantly improved photoconversion efficiencies.[6–10] As such, electrochemical properties arising from their morphology (such as the wires, tubes and rods) have facilitated the fabrication of 1D structured semiconductors and photocatalysts for the improvement of photoconversion efficiency in PECs.[11]

Although TiO_2 photocatalysts exhibit a longer electron life time and large electron diffusion length among various semiconductors, water splitting occurs under external bias (0.6 V *vs.* Normal Hydrogen Electrode, NHE) when applied as a photoelectrode in a PECs.[12,13] Moreover, most of the 1D nanostructures have been prepared with large band gap semiconductor such as TiO_2 and ZnO, which respond only in the range of ultraviolet.[8,14] Therefore 1D nanostructured materials with high

[a]Korea Center for Artificial Photosynthesis, Department of Chemistry, Sogang University, Seoul, 121-742, Republic of Korea. E-mail: yskang@sogang.ac.kr; Fax: +82 2 701 0967; Tel: +82 2 701 6379

[b]Center for Next Generation Dye-Sensitized Solar Cells and WCU, Department of Energy Engineering, Hanyang University, Seoul, 133-791, Republic of Korea

† Electronic supplementary information (ESI) available: BET and XRD data. See DOI: 10.1039/c3ta12604h

‡ These authors contributed equally to the research work.

photoconversion efficiency have been required and designed. Coupling of the lower energy band gap semiconductors such as SnO_2,[15] CdS,[16] CdTe[17] and PbSe[18] with large band gap materials such as TiO_2 and ZnO have been studied for the improvement of charge separation. The doping with other elements on TiO_2 or ZnO for the harvesting of visible light was recently applied to increase their photoelectrochemical performance.[19–21]

Recently, several groups have reported enhanced photoconversion efficiency through heterojunctions such as *p*-ZnO/*n*-TiO_2,[22] poly(phenylenevinylene)/C_{60},[23] CdTe/TiO_2,[24] and $LaVO_4$/TiO_2.[25] It is expected that the heterojunction of photoanodes facilitates the formation of charge carriers and suppresses the recombination of charge carriers at the semiconductor interface, resulting in the final high efficiency of the heterostructured photoanodes.[26]

An energetically desirable junction between $SrTiO_3$ and TiO_2 has been calculated theoretically and their improved photocatalytic properties have been widely demonstrated as heterojunction-structured photocatalysts.[27] The Kamat group reported that the heterojunction structured electrode of $SrTiO_3$ on the outer surface of TiO_2 anodized tube was approached through an exchange of cations.[28] They revealed that the coupling between the $SrTiO_3$ particle and TiO_2 nanotube offered an energetically favourable junction for the maximum amount of forward electron transfer as a promising electrode. Until now, few papers have been reported on their coupling although they are an attractive promising junction for PECs and furthermore, they have not been applied for dye-sensitized solar cells (DSSCs).

Herein, we demonstrate an N719 dye-$SrTiO_3$–TiO_2 system for an application of DSSCs using the heterostructured junction photoanode with $SrTiO_3$ on a TiO_2 nanotube array with an enlarged pore diameter for the first time. Especially, compared with $SrTiO_3$ on the outer surface of TiO_2, we have tried to approach the preferable morphology for $SrTiO_3$ on both the inner and outer surfaces of TiO_2 for an enhanced photoconversion efficiency. To the best of our knowledge, no application of the heterojunction-structured $SrTiO_3$–TiO_2 photoanode in DSSCs has been reported. Photoelectrochemical properties with controlled nanotube surface morphology were investigated in detail for application in DSSCs.

Experimental

Preparation of anodized TiO_2 nanotube arrays with enlarged pore size

In the first, pure Ti foil (99.7%, 0.25 mm thick, Sigma Aldrich) was cut into pieces of 20 × 30 mm. For the cleaning of Ti pieces, they were sequentially ultrasonicated in acetone, ethanol and distilled water for 3 min each, followed by drying with a nitrogen stream. We have slightly modified the process reported by the Grimes group.[29] The electrolytic solution for anodization was prepared with tetraethylene glycol ($C_8H_{18}O_5$, Sigma Aldrich) containing ammonium fluoride (99% NH_4F, Sigma Aldrich), 0.05 M of H_2SO_4 and distilled water. The composition of the electrolytic solution was varied to get the optimize it for morphology control of the TiO_2 nanotube under a constant applied potential for 10 h at room temperature (RT).

Two electrode cells were employed with a cleaned Ti substrate as the working electrode and with platinum foil as the counter electrode. A direct current bias (Keithley 2611 model) was performed as the voltage source for anodization and as a multimeter for measuring their current. All the anodization was carried out at RT. After the anodization, the reacted Ti substrate was washed with ethanol and distilled water. A surface cleaning to remove debris on the anodized surface would be required with ultrasonication for 3 min. Finally, anodized Ti foil was heat-treated at 450 °C for 3 h in air.

Preparation of $SrTiO_3$–TiO_2 heterojunction photoanode

In a typical experiment, we slightly modified the experimental procedure reported by P. V. Kamat group.[28] A 80 mL of $Sr(OH)_2 \cdot 8H_2O$ solution (0.025 M) was transferred to a Teflon-lined stainless steel autoclave (100 mL). The previously annealed substrate was immersed into the strontium solution in the Teflon inner. The reaction was hydrothermally performed in an electric oven under various reaction times (0.5 h, 1 h, 3 h and 5 h) at 180 °C. After the hydrothermal reaction, the reactor was removed from the electric oven and then cooled with flowing water. The reacted sample was cleaned with distilled water and then dried by nitrogen gas. To removing moisture on the reacted sample, they were kept in an oven at 100 °C.

Fabrication of dye sensitized solar cells using heterojunctioned $SrTiO_3$–TiO_2 photoanode

After cooling to RT, the hydrothermally reacted sample was immersed into a $Ru(dcbpy)_2(NCS)_2$ (dcbpy = 2,2-bipyridyl-4,4-dicarboxylato) dye solution (535-bisTBA (N719), Solaronix) with *tert*-butanol and acetonitrile (ACN, 1 : 1, v/v) at 30 °C for 18 h. After that, the dye adsorbed substrate was rinsed with ACN followed by drying in the dark. The counter electrode was prepared by spin coating of a H_2PtCl_6 solution (0.01 M in isopropyl alcohol) onto FTO glass and sintering at 450 °C for 30 min. A plastic sheet (Surlyn, 25 μm) was inserted between the photo-electrode and counter electrode as the spacer, and the space was subsequently filled with an electrolyte of 0.6 M 1-methyl-3-propylimidazolium iodide, 0.1 M LiI, 0.05 M I_2, 0.5 M *tert*-butylpyridine and 0.05 M guanidinium thiocyanate in ACN. DSSC assembly was followed as we stated in our previous report.[30]

Photoactivity and morphology characterization

The morphology and elemental composition of the samples were studied using a scanning electron microscope (SEM, JEOL) with attached energy dispersive spectroscopy (EDS) facility. For transmission electron microscopy (TEM) observations, the samples were prepared by placing one drop of the colloidal solution onto carbon coated copped grids of 200 mesh size and dried for few minutes. The porosity of the sample was evaluated using their TEM micrographs and Brunauer–Emmett–Teller (BET) measurements. To determine the crystallinity and structure of the synthesized samples, a Rigaku D'Max 2200 V (Cu K radiation, = 1.5406 Å) wide angle X-ray diffraction system was utilized. Current–voltage measurement was recorded using a PL-9 (KST-P1) with a three-electrode system which was a Pt wire

as counter electrode, Ag/AgCl as reference electrode, and NaOH solution (0.1 M) as electrolyte. Current–voltage measurements were performed under 1 sun illumination (AM 1.5, 100 mW cm^{-2}) with a Newport (USA) solar simulator (300 W Xe source) and a Keithley 2400 source meter (device area is 0.25 cm^2 with shading mask).

Results and discussions

For the formation of highly ordered TiO_2 nanotube arrays, during the initial reaction time the oxidation of Ti to Ti–O should be controlled critically by the properties of electrolyte. Electrolytes with a lower dielectric constant allow more charges to be formed on the Ti–O insulating layer.[31] After the oxidation of Ti, the dissolution reaction of Ti^{4+} from the Ti–O insulating layer should be controlled by fluoride ions in their anodizing electrolyte.[31] Then, finally, the dissolution rate *versus* reaction time reaches a constant value. So the ratio of oxidation reaction of Ti to Ti–O to the dissolution reaction of Ti–O controls critically the pore size of the TiO_2 tube. The dissolution rate of Ti to TiF_6^{2-} should be optimized by changing the molar ratio of NH_4F to H_2O during the anodization.[32] The dissolution rate is critically dependent on the mobility of the F^- ion in the different dielectric constants of electrolyte solutions of various composition.[31] Up to now, the combination and compositions of ethylene glycol have been widely reported for highly ordered TiO_2 nanotube arrays (TNTAs).[33] Even TNTAs derived from ethylene glycol systems have produced highly efficient catalytic activities, however, their morphology is not preferable for the second material in a heterojunction because of their geometric limitations. An even more preferable morphology would be required for application in heterojunctions; few researches have been reported on other combinations for the morphology control of nanotube array formation. Herein, tetraethylene glycol with a lower dielectric constant (15.7 at 25 °C) than that (37.7 at 25 °C) of ethylene glycol was used as electrolyte, along with their combination. Electrolytes with various dielectric constants were employed for the pore diameters in Fig. S1 (see ESI†).[29,31,34] For the preferential morphology of $SrTiO_3$ on the inner and outer surfaces of TNTAs, we have modified the anodization conditions through the control of the concentration of fluoride ions in the tetraethylene glycol electrolyte solution. Fig. 1 shows SEM images of anodized TiO_2 nanotube samples in a tetraethylene glycol electrolyte containing 0.3 wt% of NH_4F at a 30 V applied potential depending on various vol% of water and their typical profile of the current–time behavior during the anodization.

Compared with the anodized sample prepared at 30 vol% water content as shown in Fig. 1(a), the sample prepared at 20 vol% of water reveals the formation of nanotube arrays in the larger surface area of the Ti substrate (Fig. 1(b)). As the water content decreases from 30 to 10 vol% in the electrolyte solution, the perfect homogeneous formation of self-standing nanotube arrays was observed on the Ti substrate surface (Fig. 1(c)). Given that the mobility of the fluoride ion in electrolyte solution critically affects the dissolution rate of Ti, no TiO_2 nanotubes could be formed on the Ti substrate when the water content is higher than 30 wt% due to the high dissolution rate of Ti.[35] The TNTAs under a

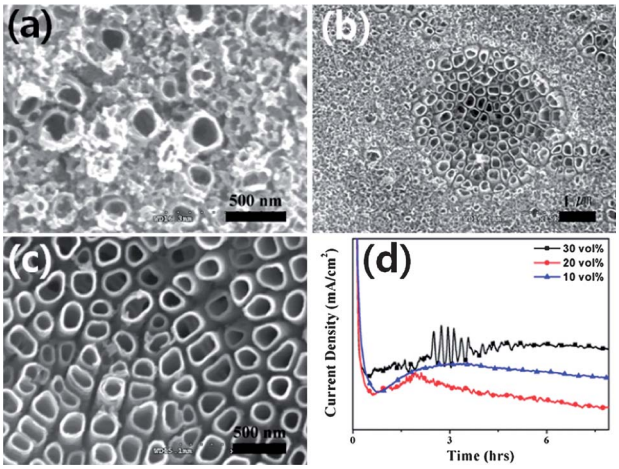

Fig. 1 SEM images of as-anodized Ti substrate in tetraethylene glycol electrolyte containing 0.3 wt% NH_4F at 30 V with 30 vol% (a), 20 vol% (b), and 10 vol% (c) of water. (d) Current–time behavior during anodization in tetraethylene glycol of electrolyte containing 0.3 wt% NH_4F and various water contents (10, 20 and 30 vol%) at 30 V.

10 vol% of water content in the electrolyte show a 150 nm pore size, 25 nm wall thickness and 1.5 μm length. The reaction rate between their dissolution and oxidation of Ti to form TiO_2 nanotubes could be explained by their current–time behavior during the anodization process. Fig. 1(d) shows a chronoamperometric curve during anodization obtained at 30 V in an electrolyte containing 0.3 wt% NH_4F with different water contents. For a 30 vol% of water, their current curve decreases sharply and then slowly increases. At a given potential, the Ti–O layer acted as an insulating layer for a few minutes and then it started to be dissolved, which is observed in Fig. 1(a), because the dissolution rate is higher the than oxidation rate of Ti metal. Hence the current slowly increased during the anodization. On the other hand, the current curve for a 10 vol% of water decreases sharply, slightly increases and then keeps constant. This indicates that a compact insulating layer of TiO_2 was formed on the surface of the Ti substrate and an equilibrium between the dissolution and oxidation of Ti metal maintained to form TNTAs. Finally, this results in a fluoride-etched Ti surface during anodization. The initially prepared TiO_2 insulating layer was continuously etched by fluoride to produce a longer and larger pore size and a compact layer could be formed on the surface of the Ti substrate in a 10 vol % of water. In the final step, constant rates were achieved for the equilibrium between dissolution of the Ti substrate and pore length growth to form a compact layer. Owing to the rate between dissolution of Ti and growth of TiO_2 nanotubes, their current–time is constant. When 0.7 wt% of NH_4F is employed, the chronoamperometric curve shows a remarkably increased current density *versus* anodization time, as shown in Fig. 2(c).

Compared with the anodized samples at 0.5 wt% of NH_4F, the higher NH_4F content at 0.7 wt% resulted in a more separated tube morphology. Their wall thickness was decreased from 40 nm (Fig. 2(a)) to 25 nm (Fig. 2(b)); a decreasing wall thickness is attributable to the increased chemical etching rate at the higher F^- concentration. It is expected that TNTAs with enlarged pore

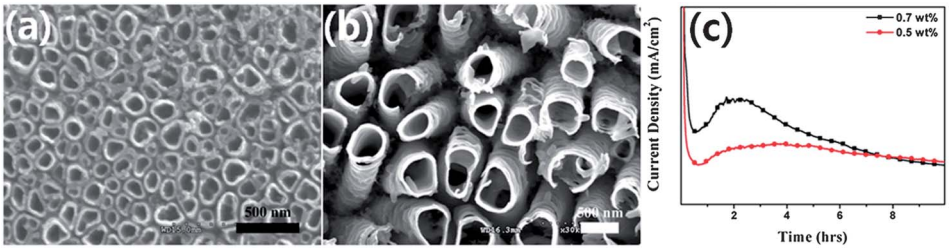

Fig. 2 SEM images of TiO_2 nanotubes obtained by (a) 0.5 wt% and (b) 0.7 wt% NH_4F in tetraethylene glycol electrolyte containing 10 vol% of water content, and (c) their current-time behavior during 30 V potential anodization.

structure are promising for decoration of secondary photocatalysts like $SrTiO_3$ nanoparticles on their surface. Compared with the many reports on Ti anodization in ethylene glycol, it is clearly noted that TNTAs with an enlarged pore structure obtained in tetraethylene glycol with a lower dielectric constant are more promising for the decoration of secondary $SrTiO_3$ nanoparticles on both the inner and outer surfaces of TiO_2 nanotubes. Fig. 3 shows clearly a different surface morphology in a comparison between SEM images of the top view and cross sectional view of bare TNTAs and ST-TNTAs.

Especially compared with the secondary materials of $SrTiO_3$ on the outer surface of TNTAs described in the previous report,[36] this approach using self-standing TiO_2 nanotube arrays with an enlarged pore structure resulted in a preferable morphology for the decoration of $SrTiO_3$ nanoparticles on both the inner and outer surfaces of TNTAs. Fig. 4(a) and (b) show TEM images with the energy dispersive spectrometer (EDS) mapping results of ST-TNTAs obtained after 1 h hydrothermal treatment. From EDS mapping lines of TEM images, $SrTiO_3$ nanoparticles were formed and dispersed on both the inner and outer surfaces of the TiO_2 nanotubes. This clearly shows the $SrTiO_3$ nanoparticles located in both inner and outer surfaces of the TiO_2 nanotubes (Fig. 4(c) and (d)). It is remarkably different from the self-standing TiO_2 nanotube with an enlarged pore compared with the ethylene glycol mediated TiO_2 nanotube in the previous report.[36]

Considering this issue, the morphology obtained by hydrothermal treatment dependent on reaction time was illustrated in Fig. 5. Their growth mechanism is supported by the SEM, EDS mapping and TEM images in Fig. 3 and 4. Fig. 5 presents SEM images of the nanotube arrays prepared with different hydrothermal reaction times. Relatively invisible small $SrTiO_3$ nanoparticles were formed on the nanotube surfaces after reaction for an initial 0.5 h as shown in Fig. 5(a). With subsequent reaction, initial small particles of $SrTiO_3$ are formed on the surface of TiO_2 tube arrays by a dissolution–precipitation process.[37]

$$TiO_2 + 2OH^- + 2H_2O \rightarrow [Ti(OH)_6]^{2-} \quad (1)$$

$$Sr^{2+} + [Ti(OH)_6]^{2-} \rightarrow SrTiO_3 + 3H_2O \quad (2)$$

$$TiO_2 + Sr(OH)_2 \rightarrow SrTiO_3 + H_2O \quad (3)$$

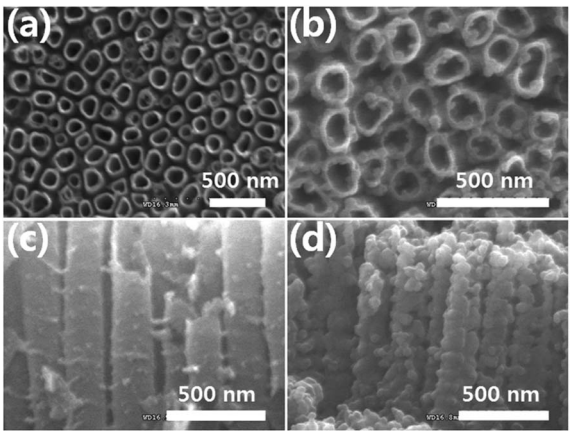

Fig. 3 SEM images of bare TiO_2 nanotube arrays: top view (a), cross sectional view (c); and $SrTiO_3$–TiO_2 heterojunction nanotube arrays: top view (b), and cross sectional view (d), after 1 h of hydrothermal treatment.

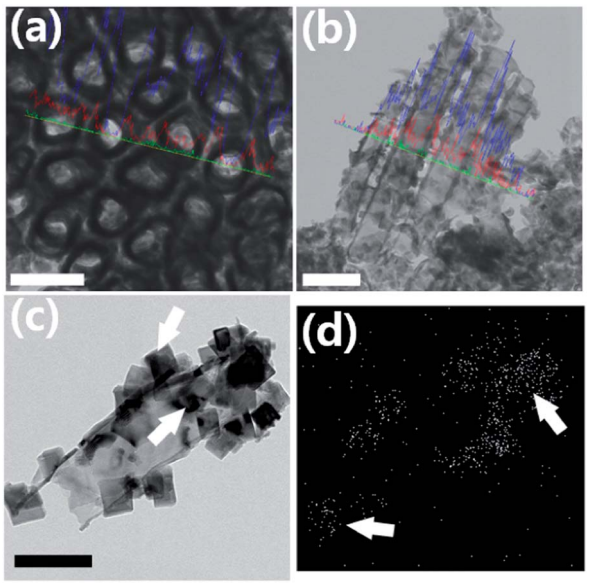

Fig. 4 HRTEM with an EDS line profile analysis of top view (a), cross view (b and c) and EDS mapping images of Sr (d) of $SrTiO_3$–TiO_2 heterojunction nanotube arrays for 1 h hydrothermal treatment (bar, 200 nm). EDS line analysis revealed the Sr elemental signal (green line) in the region of the small nanocrystallite. The Ti elemental signal (blue line) corresponds to the existence of TiO_2. The signal (red line) arising from O is derived from both $SrTiO_3$ and TiO_2.

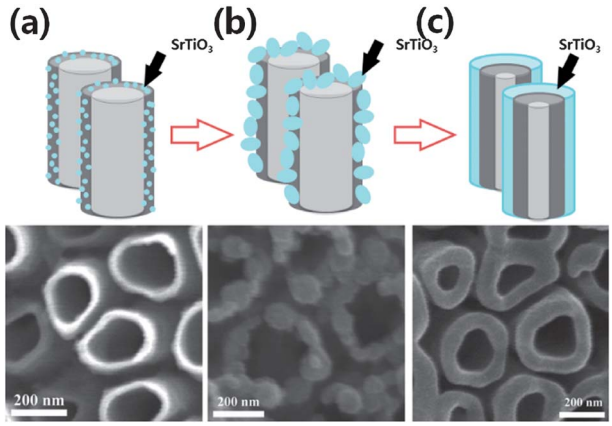

Fig. 5 Schematic drawing of $SrTiO_3$–TiO_2 heterostructured nanotube arrays depending on reaction time and their SEM images. (a) 0.5 h, (b) 1 h and (c) 3 h.

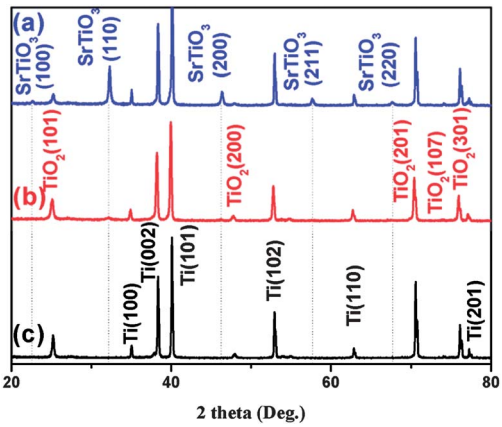

Fig. 6 X-Ray diffraction patterns of $SrTiO_3$–TiO_2 nanotube arrays prepared with hydrothermal treatment for 3 h (a) and 1 h (b), and bare TiO_2 nanotube arrays (c).

$SrTiO_3$ nucleates and grows with further reaction (eqn (3)). As the reaction time increases to 1 h, the surfaces of TNTAs begin to be covered by larger $SrTiO_3$ nanoparticles (Fig. 5(b)). A further increase of the reaction time to 3 h yields completely coated thin films of $SrTiO_3$ on TiO_2 nanotube surfaces (Fig. 5(c)). As the reaction proceeds, initially nucleated $SrTiO_3$ seed crystals begin to grow to nanoparticles on both surfaces of the TNTAs, followed by Ostwald ripening.[38] The roughness of the prepared heterostructure was changed with the formation of $SrTiO_3$ nanoparticles on the TiO_2 nanotube surfaces. The surface area of the resultant heterostructure was compared with that of anodized TiO_2 nanotube arrays by Brunauer–Emmett–Teller (BET) measurements in Fig. S2 (see ESI†).

Compared with the surface area of anodized TNTAs as 33.6 $m^2\ g^{-1}$, the values of prepared heterostructures with the hydrothermal reaction times of 0.5 h, 1 h and 3 h were determined as 34.8 $m^2\ g^{-1}$, 55.5 $m^2\ g^{-1}$ and 30.1 $m^2\ g^{-1}$, respectively. It is worth noting that their morphologies at different reaction times are well matched with roughness value variation by BET measurement.

Such behavior was clearly observed in their XRD patterns (Fig. 6 and S3 (see ESI†)). 2θ values of TNTAs in Fig. 6(c) show 25.12°, 47.78°, 73.95° and 75.96°, corresponding to (101), (200), (107) and (301) crystal planes of anatase TiO_2 (PDF#21-1272, JCPDS). After hydrothermal treatment at 180 °C for 1 h, the perovskite crystal phase of $SrTiO_3$ is observed with 2θ values of 32.30°, 46.36° and 57.64° (Fig. 6(b)). The position of diffraction peaks of 3 h reaction time shows that 2θ values around 22.72°, 32.30°, 46.36°, 57.64° and 67.63° indexing to the perovskite plane of (100), (110), (200), (211) and (220) appeared and werer matched with the XRD patterns of $SrTiO_3$ (PDF#35-0734, JCPDS). Note that the intensity of the main plane in the crystal phases of $SrTiO_3$ increases as the reaction time increases. This indicates that the $SrTiO_3$ crystalline phase gradually increases on the surface of TNTAs during the hydrothermal reaction.

The photoelectrochemical characteristics of bare TNTAs and ST-TNTAs as photoanodes were comparatively studied using 0.1 M NaOH as the electrolyte and Pt as the counter electrode. Current–voltage characteristics were recorded depending on the hydrothermal reaction time (Fig. 7 and S4 (see ESI†)). A sample prepared with a 0.5 h reaction time shows an enhanced photocatalytic property compared with the bare TiO_2 material. At 1 h reaction time, a 2.25 mA cm^{-2} current density was observed, which is 2 times higher than that of bare TNTAs. However, as their reaction time increases over 1 h, the current density decreases. The optimized electron diffusion distance at the interface between deposited $SrTiO_3$ nanoparticles and TiO_2 nanotubes was obtained with 1 h reaction time by increasing the forward electron diffusion and suppressing backward electron diffusion from TiO_2 nanotubes to $SrTiO_3$ nanoparticles. Considering the heterojunction between semiconductors with different conduction band energies, the photoinduced electron transfer efficiency is critically dependent on the electron transfer (diffusion) distance between the electron donor and acceptor, the energy barrier for the electron transfer through the interface and the contacting surface area between them. In the case of too-short electron transfer distance, more electrons are allowed to be transported (in the back direction) toward the electron donor. This also results in a lower energy barrier for the electron transfer, both forward and backward. The optimized electron transport energy barrier of the interface and electron transfer distance could be obtained from the 1 h hydrothermal reaction for the $SrTiO_3$ nanoparticle formation. So, the recombination will occurring dominantly. In this respect, the single particle size of $SrTiO_3$ is related to the interfacial area and distance.

With SEM and XRD results from Fig. 5 and 6, it is clear that $SrTiO_3$ is nucleated and grown on the surface of TiO_2 nanotubes. This means that the surface area of $SrTO_3$, and the optimized interfacial area and distance between $SrTiO_3$ and TiO_2 would be critical factors for the high photocurrent value of heterostructured ST-TNTAs photoanodes. Fig. 7(b) reveals the highest photocurrent values of the ST-TNTAs heterostructure is at a 1 h reaction time compared to the less-coated (0.5 h) and the completely-coated (3 h) layer of $SrTiO_3$ on TNTAs. Their enhanced photoactivity is also possible at higher electron–hole

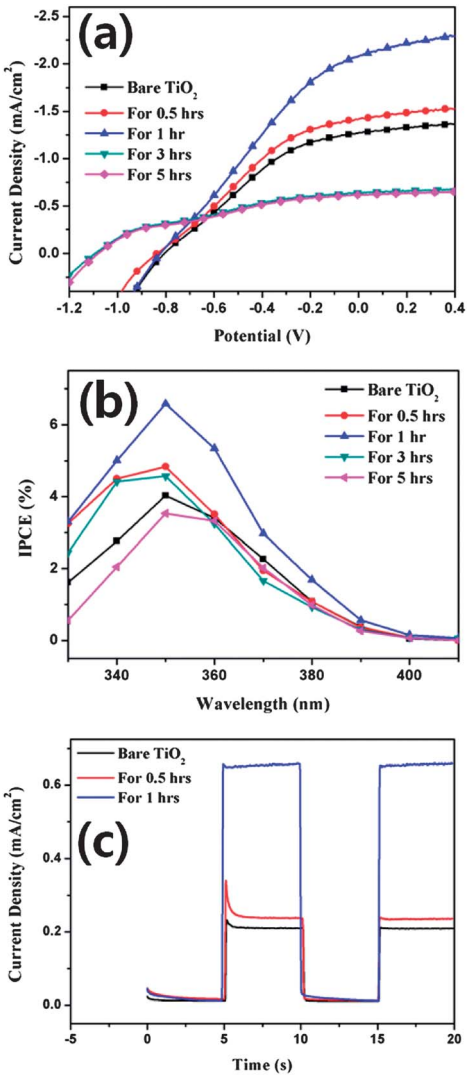

Fig. 7 (a) Current–voltage characteristics and (b) IPCE spectra under no applied external bias under illumination of one sun. (c) Photoresponse of electrode recorded depending on hydrothermal reaction time. UV light (UV 250 nm–385 nm) was employed as the light source.

separation because of the larger surface area at the interface between $SrTiO_3$ and TiO_2. This is possible by suppressing the recombination of charge carriers at the interface. Considering this issue, the coupling between $SrTiO_3$ and TiO_2 facilitates the electron and hole separation by the larger surface area and results in their onset potential to be more negative and the improvement of their current density. However, the current–voltage value decreases as the hydrothermal reaction time increases to longer than 1 h. It is assumed that the larger interfacial area and shorter contact distance between the secondary $SrTiO_3$ nanoparticle and the TiO_2 surface at 3 h of hydrothermal reaction time would allow more charge recombination sites and finally result in a decrease of charge transfer by allowing more charge recombination. It is clear that their current density decreases although their onset potential is shifted more negatively when the hydrothermal reaction time employed is longer than 1 h. Consequently, the hydrothermal reaction time for 1 h provides an optimized contact distance between the $SrTiO_3$ nanoparticles and the TiO_2 interface, and the largest surface area for the adsorption of dye molecules on the surface of photoanodes. This allows an optimized contact area between $SrTiO_3$ nanoparticle and TiO_2 interface for better diffusion of electrons and holes through the interface. The maximum efficiencies of $SrTiO_3$–TiO_2 with 0.5 h, 1 h, 3 h and 5 h are 4.8%, 6.6%, 4.5% and 3.5%, respectively, in comparison to 4.0% for bare TiO_2 nanotube arrays. The improved photoconversion efficiency for hetero-structured ST-TNTAs for 1 h reaction is matched with the largest surface area as shown in Fig. 7 and S2 (see ESI†).

Heterostructured ST-TNTAs were applied as a photoanode for photoelectrochemical cells. For the DSSC preparation, dyes were adsorbed on the surfaces of $SrTiO_3$–TiO_2 nanotube arrays by immersion in a 0.3 mM of N719 dye for 18 h. Their photocurrent density and photovoltage curves were recorded under 1 sun illumination (AM 1.5, 100 mW cm^{-2}) and shown in Fig. 8(a). DSSC with bare TiO_2 nanotube arrays showed 0.18%, 0.609 V, 0.428 mA cm^{-2} and 67.72% as photoconversion efficiency, open circuit voltage (V_{oc}), short circuit current density (J_{sc}) and fill factor (FF), respectively. Interestingly, when the heterostructured ST-TNTAs were applied as photoanodes in DSSCs, 0.48% photoconversion efficiency is achieved with 0.708 V of V_{oc}, 1.08 mA cm^{-2} of J_{sc} and 62.30% of FF. This indicates that the ST-TNTAs heterostructured junction allowed the photoconversion efficiency, V_{oc} and J_{sc} to be enhanced with

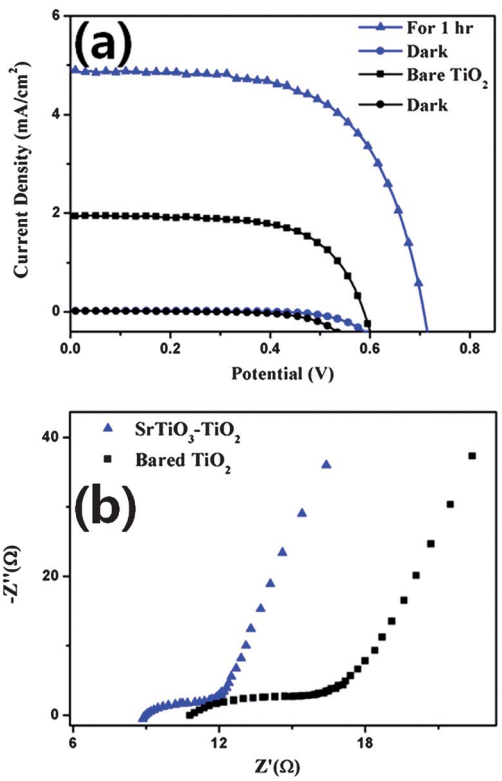

Fig. 8 (a) *J–V* characteristics of DSSCs using $SrTiO_3$–TiO_2 hetero-structured nanotube arrays under simulated AM 1.5 light illumination. (b) Electrochemical impedance spectra of bare TiO_2 tube array and $SrTiO_3$–TiO_2 heterostructured tube arrays.

the ST-TNTAs heterostructured photoanode in DSSCs. Compared with the photovoltaic characteristics of TiO_2 nanotube arrays, the photovoltaic performance is clearly improved by promoting charge transport *via* the heterostructured $SrTiO_3$–TiO_2 photoanode cell system.

Electrochemical impedance spectroscopy (EIS) was measured to evaluate the electrochemical characteristics in this DSSC system (Fig. 8(b)). EIS is a powerful tool to study the kinetics of charge transfer.[39] EIS results of bare TiO_2 tube arrays and $SrTiO_3$–TiO_2 heterostructure show an arc in the higher frequency region and a straight line in the lower frequency region. The first arc in DSSC is attributed to the charge-transfer resistance from the electrode.[39] The resistance values of the electrode were 6 Ω and 4 Ω for bare TNTAs and ST-TNTAs, respectively. It is noted that the $SrTiO_3$–TiO_2 heterojunction electrode has good efficiency of charge transfer showing a lower resistance than that of the bare TiO_2 tube electrode. Also, the $SrTiO_3$ nanoparticles/TNTAs interface allows a lower energy barrier for the electron transfer compared with TiO_2 nanoparticle/TNTAs. The lower resistance value of $SrTiO_3$ nanoparticles/TNTAs compared to TiO_2 nanoparticles/TNTAs is well shown in Fig. 8(b).[40] This indicates that $SrTiO_3$ nanoparticles/TNTAs have a lower energy barrier for electron transfer through the interface than TiO_2 nanoparticle/TNTAs.

The energy band diagram of the components in DSSCs using a $SrTiO_3$–TiO_2 heterostructured photoanode is shown in Fig. 9. The valence band (VB) of $SrTiO_3$ is positioned under the lowest unoccupied molecular orbital (LUMO) level of the N719 dye and is located simultaneously above the conduction band (CB) of the TiO_2 nanotube arrays.[41] The VB of $SrTiO_3$ is positioned above that of TNTAs and also lies under the highest occupied molecular orbital (HOMO) level of the N719 dye. It is noted that an excited electron from the HOMO level to the LUMO level in N719 dye is injected to the CB of $SrTiO_3$ particles and sequentially transferred to the CB of TNTAs in the working process of DSSCs. The transfer process of charge carriers is thermodynamically more favourable from a higher LUMO level of the N719 to the conduction band of TiO_2 by suppressing charge recombination due to the junction with $SrTiO_3$ nanoparticles.

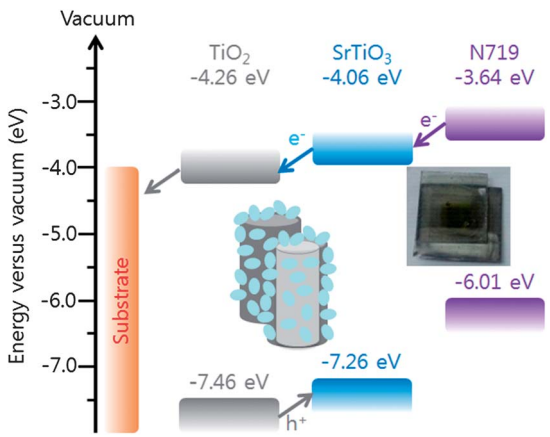

Fig. 9 Energy band diagram of the N719 dye, $SrTiO_3$ and TiO_2 as components of dye-sensitized solar cells, with reference with the vacuum level.

This clearly matches with the EIS result in Fig. 8. The photocurrent density is determined as the efficiency of electron transfer from the adsorbed N719 dye molecule to the photoanode *via* $SrTiO_3$ nanoparticles. The electron transfer from the N719 dye molecule to $SrTiO_3$ occurred by photoinduced long range electron transfer. The electron transfer from $SrTiO_3$ to TiO_2 occurred by a diffusion controlled process. Both of the processes are critically dependent on the electron transfer distance between the donor and acceptor. The electron transfer between the N719 dye and $SrTiO_3$ is not dependent on the contact area, but the diffusion controlled electron transfer between $SrTiO_3$ and TiO_2 is critically dependent on the contact area at the interface between them. Their energy band diagram shows that N719 dye-$SrTiO_3$–TiO_2 system gives favourable charge separation and a higher efficiency of electron transfer.

Conclusions

In summary, we have developed an N719 dye-$SrTiO_3$–TiO_2 system for application in DSSCs. The N719 dye-$SrTiO_3$–TiO_2 system is thermodynamically more favourable for electron transport and charge separation. For the heterostructure junction of $SrTiO_3$–TiO_2 nanotube arrays, $SrTiO_3$ was synthesized on newly proposed TiO_2 nanotube arrays with an enlarged pore structure with 150 nm, 25 nm and 1.5 μm as their pore size, wall thickness and length, in a water–NH_4F–tetraethylene glycol system. The nanotube arrays with an enlarged pore structure are the preferable morphology for secondary reaction of $SrTiO_3$ nanoparticles on both the inner and outer surfaces of TiO_2 nanotube arrays for photoconversion activity. Compared with the photovoltaic characteristic of bare TiO_2 nanotube arrays, DSSCs with an $SrTiO_3$–TiO_2 heterojunction electrode have shown an improved photoelectrochemical performance because of their charge separation and suppression of charge recombination from $SrTiO_3$ on TiO_2 nanotube arrays. We expect this successful synthetic approach should be preliminary evidence for other titanate structures for application in PECs with improved photoconversion efficiency.

Acknowledgements

This work was supported by the National Research Foundation of Korea (NRF) grant funded by the Korea government (MSIP) for the Center for Next Generation Dye-sensitized Solar Cells (No. 2008-0061903).

Notes and references

1 A. Fujishima and K. Honda, *Nature*, 1972, **238**, 37.
2 A. Mao, G. Y. Han and J. H. Park, *J. Mater. Chem.*, 2010, **20**, 2247; J. Gan, X. Lu, T. Zhai, Y. Zhao, S. Xie, Y. Mao, Y. Zhang, Y. Yang and Y. Tong, *J. Mater. Chem.*, 2011, **21**, 14685; C.-S. Lim, S. H. Im, J. H. Rhee, Y. H. Lee, H.-J. Kim, N. Maiti, Y. Kang, J. A. Chang, M. K. Nazeeruddin, M. Grätzel and S. I. Seok, *J. Mater. Chem.*, 2012, **22**, 1107; J. Yang, W. Li, J. Li, D. Sun and Q. Chen, *J. Mater. Chem.*, 2012, **22**, 17744.

3 Y. Xia, P. Yang, Y. Sun, Y. Wu, M. Brian, B. Gates, Y. Yin, F. Kim and H. Yan, *Adv. Mater.*, 2003, **15**, 353; G. K. Mor, K. Shankar, M. Paulose, O. K. Varghese and C. A. Grimes, *Nano Lett.*, 2005, **5**, 191; K. Shankar, I. J. Basham, N. K. Allam, O. K. Varghese, G. K. Mor, X. Feng, M. Paulose, A. S. Jason, K. S. Choi and C. A. Grimes, *J. Phys. Chem. C*, 2009, **113**, 6327.
4 F. E. Osterloh, *Chem. Soc. Rev.*, 2013, **42**, 2294; R. K. Joshi and J. J. Schneider, *Chem. Soc. Rev.*, 2012, **41**, 5285.
5 A. J. Frank, N. Kopidakis and J. V. D. Lagemaat, *Coord. Chem. Rev.*, 2004, **248**, 1165.
6 M. Law, L. E. Greene, J. C. Johnson, R. Saykally and P. Yang, *Nat. Mater.*, 2005, **4**, 455.
7 K. Zhu, N. R. Neale, A. Miedaner and A. J. Frank, *Nano Lett.*, 2007, **7**, 69.
8 G. K. Mor, K. Shankar, M. Paulose, O. K. Varghese and C. A. Grimes, *Nano Lett.*, 2006, **6**, 215.
9 J. Wei, Y. Jia, Q. Shu, Z. Gu, K. Wang, D. Zhuang, G. Zhang, Z. Wang, J. Luo, A. Cao and D. Wu, *Nano Lett.*, 2007, **7**, 2317.
10 E. Kymakis and G. A. J. Amaratunga, *Appl. Phys. Lett.*, 2002, **80**, 112.
11 Y.-Z. Long, M. Yu, B. Sun, C.-Z. Gu and Z. fan, *Chem. Soc. Rev.*, 2012, **41**, 4560; H. M. Chen, C. K. Chen, R.-S. Liu, L. Zhang, J. Zhang and D. P. Wilkinson, *Chem. Soc. Rev.*, 2012, **41**, 5654; M. Yu, Y.-Z. Long, B. Sun and Z. Fan, *Nanoscale*, 2012, **4**, 2783.
12 M. Quintana, T. Edvinsson, A. Hagfeldt and G. Boschloo, *J. Phys. Chem. C*, 2007, **111**, 1035.
13 A. L. Linsebigler, G. Lu and J. T. Yates, *Chem. Rev.*, 1995, **95**, 735.
14 X. Chen and S. S. Mao, *Chem. Rev.*, 2007, **107**, 2891.
15 X. Wu, S. Zhang, L. Wang, Z. Du, H. Fang, Y. Ling and Z. Huang, *J. Mater. Chem.*, 2012, **22**, 11151.
16 Y. Tak, S. J. Hong, J. S. Lee and K. Yong, *J. Mater. Chem.*, 2009, **19**, 5945.
17 X. Wang, H. Zhu, Y. Xu, H. Wang, Y. Tao, S. Hark, X. Xiao and Q. Li, *ACS Nano*, 2010, **4**, 3302.
18 R. D. Schaller and V. I. Klimov, *Phys. Rev. Lett.*, 2004, **92**, 186601.
19 W. T. Sun, Y. Yu, H. Y. Pan, X. F. Gao, Q. Chen and L. M. Peng, *J. Am. Chem. Soc.*, 2008, **130**, 1124.
20 Y. Lee and Y. Lo, *Adv. Funct. Mater.*, 2009, **19**, 604.
21 J. H. Bang and P. V. Kamat, *Adv. Funct. Mater.*, 2010, **20**, 1970.
22 L. Lin, Y. Yang, L. Men, X. Wang, D. He, Y. Chai, B. Zhao, S. Ghoshroy and Q. Tang, *Nanoscale*, 2013, **5**, 588.
23 H. Mattoussi, M. F. Rubner, F. Zhou, J. Kumar, S. K. Tripathy and L. Y. Chiang, *Appl. Phys. Lett.*, 2000, **77**, 1540.
24 M. Zhang, Y.-N. Wang, E. Moulin, D. Grützmacher, C.-J. Chien, P.-C. Chang, X. Gao, R. Carius and J. G. Lu, *J. Mater. Chem.*, 2012, **22**, 10441.
25 H. Huang, D. Li, Q. Lin, W. Zhang, Y. Shao, Y. Chen, M. Sun and X. Fu, *Environ. Sci. Technol.*, 2009, **43**, 4164.
26 J. A. Seabold, K. Shankar, R. H. T. Wilke, M. Paulose, O. K. Varghese, C. A. Grimes and K. S. Choi, *Chem. Mater.*, 2008, **20**, 5266.
27 P. Reunchan, S. Ouyang, N. Umezawa, H. Xu, Y. Zhang and J. Ye, *J. Mater. Chem. A*, 2013, **1**, 4221; A. M. Schultz, P. A. Salvador and G. S. Rohrer, *Chem. Commun.*, 2012, **48**, 2012; J. Ng, S. Xu, X. Zhang, H. Y. Yang and D. D. Sun, *Adv. Funct. Mater.*, 2010, **20**, 4287.
28 J. Zhang, J. H. Bang, C. Tang and P. V. Kamat, *ACS Nano*, 2010, **4**, 387.
29 N. K. Allam and C. A. Grimes, *Langmuir*, 2009, **25**, 7234.
30 S. Das, P. Sudhagar, V. Verma, D. Song, E. Ito, S. Y. Lee, Y. S. Kang and W. B. Choi, *Adv. Funct. Mater.*, 2011, **21**, 3729.
31 K. Shankar, G. K. Mor, H. E. Prakasam, S. Yoriya, M. Paulose, O. K. Varghese and C. A. Grimes, *Nanotechnology*, 2007, **18**, 065707.
32 J. M. Macak, H. Tsuchiya, A. Ghicov, K. Yasuda, R. Hahn, S. Bauer and P. Schmuki, *Curr. Opin. Solid State Mater. Sci.*, 2007, **11**, 3; P. Roy, S. Berger and P. Schmuki, *Angew. Chem., Int. Ed.*, 2011, **50**, 2904.
33 Y. Xiong, L. Tao, H. Liu and W. Shen, *J. Mater. Chem. A*, 2013, **1**, 783; L. Tao, Y. Xiong, H. Liu and W. Shen, *J. Mater. Chem.*, 2012, **22**, 7863.
34 S. Yoriya and C. A. Craig, *J. Mater. Chem.*, 2011, **21**, 102; S. Yoriya, W. Kittimeteeworakul and N. Punprasert, *J. Chem. Chem. Eng.*, 2012, **6**, 686; S. Yoriya and C. A. Craig, *Langmuir*, 2010, **26**, 417; R. Kojima, Y. Kimura, M. Bitoh, M. Abe and M. Niwano, *J. Electrochem. Soc.*, 2012, **159**, D629.
35 J. Wang and Z. Lin, *J. Phys. Chem. C*, 2009, **113**, 4026; K. Shankar, G. K. Mor, A. Fitzgerald and C. A. Grimes, *J. Phys. Chem. C*, 2007, **111**, 21.
36 Y. Hou, X. Li, Q. Zhao, X. Quan and G. Chen, *Environ. Sci. Technol.*, 2010, **44**, 5098.
37 Y. Xin, J. Jiang, K. Huo, T. Hu and P. K. Chu, *ACS Nano*, 2009, **3**, 3228.
38 T. Cao, Y. Li, C. Wang, C. Shao and Y. Liu, *Langmuir*, 2011, **27**, 2946.
39 F. Fabregat-Santiago, J. Biquert, G. Garcia-Belmonte, G. Boschloo and A. Hagfeldt, *Sol. Energy Mater. Sol. Cells*, 2005, **87**, 117; Q. Wang, J. E. Moser and M. Gratzel, *J. Phys. Chem. B*, 2005, **109**, 14945.
40 T.-H. Meen, Y.-T. Jhuo, S.-M. Chao, N.-Y. Lin, L.-W. Ji, J.-K. Tsai, T.-C. Wu, W.-R. Chen, W. Water and C.-J. Huang, *Nanoscale Res. Lett.*, 2012, **7**, 579.
41 I. Chung, B. Lee, J. He, R. P. H. Chang and M. G. Kanatzidis, *Nature*, 2012, **485**, 486; Q. Wang, J. E. Moser and M. Gratzel, *J. Phys. Chem. B*, 2005, **109**, 14945.